Observability-Based Path-Planning and Flow-Relative Control of a Bioinspired Sensor Array in a Karman Vortex Street

Brian Free, Mukund K. Patnaik, and Derek A. Paley

***Abstract*— This paper describes the use of a bioinspired array of pressure sensors to estimate and control flow-relative position using potential flow theory and a recursive Bayesian filter. Inspired by the lateral-line neuromasts found in fish, the sensing scheme is validated using off-the-shelf pressure sensors. First, the strength and location of a stationary spiral vortex are estimated and closed-loop control of relative position is demonstrated experimentally. Second, we identify an optimal path through a Karman vortex street using empirical observability. Finally, the vorticity and location of the Karman vortex street is estimated and closed-loop control to the optimal path is demonstrated experimentally. This work is a precursor to an autonomous robotic fish sensing the wake of another fish and/or performing pursuit and schooling behavior.**

I. Introduction

Autonomous underwater navigation in and through complex structures requires a sensing system capable of perceiving variable flow patterns. Inspiration arises from a fish-sensing system known as the lateral line, which contains superficial and canal neuromasts sensitive to flow velocity and pressure gradients, respectively [1],[2]. Fish use the lateral line to help locate prey, even in complete darkness [3]. Bioinspired sensing schemes that use pressure-sensing modalities have the potential to enable robotic platforms to estimate the location and strength of circulating flow structures such as vortices.

This manuscript describes the use of off-the-shelf pressure sensors to estimate the location of a spiral vortex and implement (one-dimensional) closed-loop control of its position relative to a linear sensor array. Additionally, a square pressure-sensor array in a Karman vortex street is actuated in the cross-stream direction in order to follow an optimal path determined by empirical observability. A Karman vortex street is the pattern of clockwise and counter-clockwise vortices shed by a blunt body due to flow separation. This pattern also occurs in the wake of fish as they swim [4], and is investigated here as a precursor to fish-robot pursuit of other fish robots and/or schooling behavior.

This work is supported by the Office of Naval Research under Grant No. N000141512246. Brian Free is also supported by the National Science Foundation Graduate Research Fellowship Program under Grant No. DGE 1322106.

Brian Free is a Graduate Research Assistant in the Department of Aerospace Engineering at the University of Maryland, College Park, MD, 20742, USA. bfree@umd.edu

Mukund K. Patnaik is an undergraduate researcher in the Department of Aerospace Engineering at the University of Maryland, College Park, MD, 20742, USA. mpatnaik@terpmail.umd.edu

Derek A. Paley is the Willis H. Young Jr. Associate Professor of Aerospace Engineering Education in the Department of Aerospace Engineering and the Institute for Systems Research, University of Maryland, College Park, MD 20742, USA. dpaley@umd.edu

In prior work on artificial lateral lines, Lagor et al. demonstrated estimation of flowspeed and angle of attack of a fish-shaped body submerged in uniform flow using commercial pressure sensors [5]. DeVries et al. utilized bi-modal sensing with traditional pressure sensors combined with ionic polymer-metal compositites (IPMC) sensors in order to estimate the location of an upstream obstacle and orient a fish robot in uniform flow [6]. Fernandez estimated vortex location using only pressure sensors, but performed no closed-loop control [7]. Ren and Mohseni use the potential flow model of a vortex street to examine the effects flow has on the lateral line of a fish but performed no flow estimation [8]. Lagor et al. used the local unobservability index to determine the best paths to tour a two-vortex system [9]. Li and Saimek used pressure sensors on a submerged airfoil to estimate vortex strength only using a Kalman filter [10]. To the authors' knowledge, there has been no prior work on estimating the location of moving vortices with pressure sensor arrays or optimal-path tracking in a vortex street.

Estimates of the location and strength of a spiral vortex and a vortex street are formed using pressure measurements from an artificial lateral line and used in closed-loop control. The technical approach utilizes tools from potential flow theory, nonlinear estimation, and nonlinear observability. The spiral vortex is modeled as an irrotational and incompressible flow composed of the superposition of a sink and a point vortex. The Karman vortex street is modeled as two parallel infinite lines of vortices [11]. Measurement equations output the predicted pressure reading according to four states (sink strength, vortex strength, and planar coordinates) in the spiral vortex case and three states (vortex strength and planar coordinates) in the Karman vortex street case. All calculations are performed in a reference frame fixed to the sensor array. These equations, in conjunction with the actual sensor readings, are used in a nonlinear recursive Bayesian framework to estimate the states. For the spiral vortex, the estimated vortex position is used in a proportional feedback controller that actuates the sensor array to drive (one component of) the relative position to zero. For the vortex street, the estimate is used in feedback control to track an optimal reference trajectory pre-determined by empirical observability. Traditional observability answers the question "can the system's states be recreated from the measurements?" and often requires taking Lie derivatives of the system dynamics and evaluating the observability rank condition. Empirical observability instead gives a measure of how easily observed a system is and requires only the ability to simulate the system dynamics [12].

The contributions of this paper are (1) a Bayesian filter framework using pressure measurements to estimate vortex strength and location in static and moving patterns including a stationary spiral vortex and a Karman vortex street; (2) calculation of an optimal path through a vortex street based on empirical observability; and (3) closed-loop control of a sensor array relative to a static spiral vortex and along the optimally observable path through a vortex street. This work demonstrates an artificial lateral line sensing variable flow structures, which has applications in autonomous underwater navigation in cluttered environments and sensing other fish or robots in the water.

The paper proceeds as follows. Section II provides technical background in potential flow theory, nonlinear estimation, and empirical observability. Section III presents the model of the sensor array, the corresponding measurement equations, and empirical observability-based path-planning. Section IV describes results from the experimental testbeds and Section V summarizes the paper and ongoing work.

II. Background

A. Modeling and Measuring Vortex Flows

Potential flow allows the flow velocity at any point to be calculated from a single function; it is used here to model the flow field induced by vortical flow structures. A spiral vortex, such as that created in a bathtub drain, is represented as an ideal sink combined with a point vortex. Let $z \in \mathbb{C}$ be a point in the complex plane. The complex potential of a spiral vortex $F_{sv}(z)$ is[1] [13]

$$F_{sv}(z) = \frac{\Lambda}{2\pi}\log(z-z_0) - \mathbf{j}\frac{\Gamma}{2\pi}\log(z-z_0), \tag{1}$$

where Λ is the source strength (negative for a sink), Γ is the vortex strength, and $z_0 \in \mathbb{C}$ is the location of the vortex center. The velocity field is the conjugate of the gradient of the complex potential, i.e.,

$$W_{sv}(z) = \left(\frac{dF_{sv}}{dz}\right)^* = \left(\frac{\Lambda}{2\pi(z-z_0)} - \mathbf{j}\frac{\Gamma}{2\pi(z-z_0)}\right)^*. \tag{2}$$

A Karman vortex street in freestream flow with primary vortex located at $z_0 = x_0 + \mathbf{j}y_0$ in a moving sensor frame has the potential [11]

$$F_{kvs}(z) = Uz + \mathbf{j}\frac{\gamma}{2\pi}\Bigg[\log\sin\frac{\pi}{a}(z-z_0) - \log\sin\frac{\pi}{a}(z-(\frac{1}{2}a+\mathbf{j}h)-z_0)\Bigg], \tag{3}$$

where γ, a, h, and U are the vortex strength, horizontal spacing of the vortices, vertical spacing of the vortices, and freestream speed of the flow, respectively. The velocity field is again the conjugate of the gradient of the potential [13]

$$W_{kvs}(z) = \left(\frac{dF_{kvs}}{dz}\right)^* = \Bigg(U + \mathbf{j}\frac{\gamma}{2a}\Bigg[\cot\frac{\pi}{a}(z-z_0) - \cot\frac{\pi}{a}(z-(\frac{1}{2}a+\mathbf{j}h)-z_0)\Bigg]\Bigg)^*. \tag{4}$$

The real and imaginary components of this term are the horizontal and vertical velocities induced by the flow.

The velocities modeled above can be used with Bernoilli's equation to calculate the pressure that would be sensed at a particular location. Let $p(z)$ denote the static pressure at z, ρ the fluid density, $W(z)$ the velocity at z, g the gravitational acceleration, and H the elevation. To model the pressure sensed at z, apply Bernoulli's principle [14], which for steady, inviscid, incompressible, irrotational flow, yields the constant

$$C = p(z) + \frac{1}{2}\rho|W(z)|^2 + \rho g H. \tag{5}$$

B. Bayesian Estimation and Observability

A Bayesian filter assimilates measurements to estimate unknown states such as vortex location and strength. Equations (2), (4), and (5) are used in Section III to model pressure measurements from the sensors. A recursive, grid-based Bayesian filter estimates a set $\mathbf{X}$ of parameters from a set $\mathbf{Y}$ of measurements [15]. Suppose the measurement vector is

$$\mathbf{Y} = \mathscr{H}(\mathbf{X}) + \eta,$$

where $\mathscr{H}(\mathbf{X})$ is the (nonlinear) measurement equation and η is Gaussian sensor noise. In this case, the conditional probability of measurement $\mathbf{Y}$ given state vector $\mathbf{X}$ is

$$\pi(\mathbf{Y}|\mathbf{X}) = \frac{1}{\sqrt{(2\pi)^n \det(R)}}\exp\left[-\frac{1}{2}(\mathbf{Y}-\mathscr{H}(\mathbf{X}))^T R^{-1}(\mathbf{Y}-\mathscr{H}(\mathbf{X}))\right], \tag{6}$$

where n is the number of measurements and $R \in \mathbb{R}^{n \times n}$ is the covariance matrix of the sensor noise. In practice, a discrete grid may be used to evaluate the measurement equation, which, for $\mathbf{X} \in \mathbb{R}^n$, implies an n-dimensional grid is needed. (For a large number of grid points, this calculation may be computationally intensive.)

Bayesian estimation combines the prior estimate with the measurement likelihood to form a posterior estimate via Bayes' formula,

$$\pi(\mathbf{X}|\mathbf{Y})_{posterior} = \kappa\pi(\mathbf{Y}|\mathbf{X})\pi(\mathbf{X})_{prior}, \tag{7}$$

where κ is a normalizing factor to ensure the posterior integrates to one. After each time step, the posterior becomes the prior and the process is repeated with a new measurement. (A uniform prior is used for the initial time step.)

Observability is a concept that quantifies the ability of states $\mathbf{X}$ to be estimated from measurements $\mathbf{Y}$. Krener and Ide construct the idea of the *empirical observability gramian* W_o in [12]. For the nonlinear system

$$\dot{\mathbf{X}} = f(t,\mathbf{X}) \text{ and } \mathbf{Y} = \mathscr{H}(t,\mathbf{X}),$$

[1] To avoid confusion with index j, bold $\mathbf{j} = \sqrt{-1}$ is used to indicate the imaginary number.

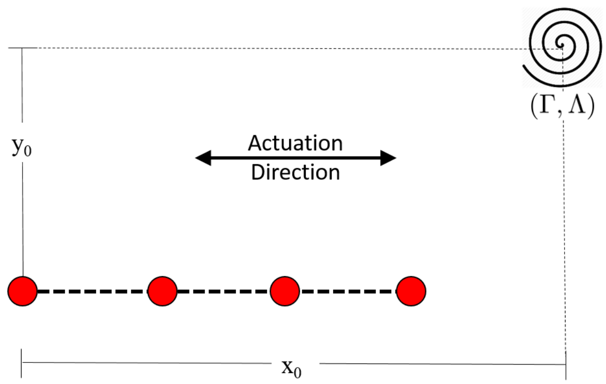

Fig. 1: Illustration of sensor and control system for the spiral vortex case. Red circles are pressure sensors. The origin of the sensor frame is the leftmost pressure sensor. The vortex is located at (x_0, y_0) in the sensor frame and has sink strength Λ and vortex strength Γ. The spiral vortex is fixed in the inertial frame; the array actuates left and right, changing x_0.

$$W_o(i,j) = \frac{1}{4\varepsilon^2}\int_0^T (\mathbf{Y}^{+i} - \mathbf{Y}^{-i})^\top (\mathbf{Y}^{+j} - \mathbf{Y}^{+j})dt, \quad (8)$$

where $\mathbf{Y}^{\pm i}$ is the measurement produced from the state $\mathbf{X}^{\pm i} = \mathbf{X} \pm \varepsilon \mathbf{e}^i$, and $\varepsilon \mathbf{e}^i$ is a small perturbation along the i^{th} unit vector in $\mathbb{R}^n$, with $i = 1, \ldots, n$. The inverse of the minimum singular value of W_o on a time interval $[0, T]$ is the *local unobservability index*, $\nu = 1/\sigma_{min}(W_o)$. This metric is dependent on specific experimental conditions such as sensor placement, sensor number, vortex strength, etc., and therefore cannot be used to compare observability between different configurations. However, it is useful for comparing paths through a field using the same experimental configuration. The path with the lowest unobservability index will lead to the best estimate of the parameter space.

III. Modeling and Control

A. State-Space Modeling

Forming the measurement equations for the spiral vortex and the vortex street requires understanding the physical setup in each case. Figure 1 depicts the configuration of the sensing and control system for the spiral vortex and Figure 2 depicts the configuration of the sensing and control system for the Karman vortex street. A straight, 30 cm long sensor array is used for the spiral vortex to provide widely varied measurements to properly test the estimator. A 6 cm square sensor array is used for the Karman vortex street to better to fit the experimental testbed described in Section 4. In both cases, potential flow theory and Bernouilli's principle are used to model the static pressure $p(z)$. In order to remove the effects of ambient pressure, differences between pairs of pressure sensors are measured and modeled, analogous to how canal neuromasts function [16]. From (5), for any two sensor locations z_i and z_j, we have

$$p(z_i) + \frac{1}{2}\rho|W(z_i)|^2 = p(z_j) + \frac{1}{2}\rho|W(z_j)|^2.$$

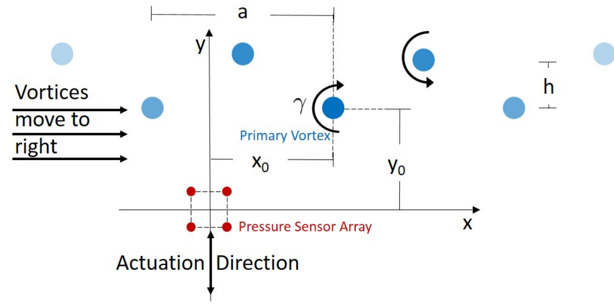

Fig. 2: Illustration of sensor and control system for the Karman vortex street. Red circles are pressure sensors. The origin of the sensor frame is in the center of the pressure sensor array. The closest clockwise vortex to the sensor array is referred to as the primary vortex and has coordinates (x_0, y_0) in the sensor frame. Each vortex has strength γ and the vortex street moves to the right with speed U. Every like-signed vortex in the street is spaced horizontally by a units. The two lines of vortices are separated vertically by h units. The array moves vertically in the cross-stream direction.

The pressure difference, $\Delta p_{ij} = p(z_i) - p(z_j)$, is

$$\Delta p_{ij} = \frac{1}{2}\rho\left[|W(z_j)|^2 - |W(z_i)|^2\right].$$

Using (2) yields

$$\Delta p_{ij} = \frac{\rho(\Lambda^2 + \Gamma^2)}{8\pi^2}\left[\frac{1}{|z_j - z_0|^2} - \frac{1}{|z_i - z_0|^2}\right] \quad (9)$$

in the spiral vortex case. The equation for the vortex street case is omitted for space constraints; it is a function of sensor position, street position, street spacing, and vortex strength.

With the measurement equations formed, the Bayesian filter framework for these experiments can be put in place. For n_{ps} pressure sensors, there are $n_p = (n_{ps}^2 - n_{ps})/2$ measurements of pressure differences and the measurement vector is

$$\mathbf{Y} = [\Delta p_1, \ldots, \Delta p_{n_p}]^T \in \mathbb{R}^{n_p}.$$

Note that there are only $n-1$ linearly independent pressure differences. Using redundant measurements in the Bayesian filter reduces the effect of measurement noise more quickly at the cost of running fewer times per second. In the spiral vortex case, the state vector is

$$\mathbf{X}_{sv} = [\Re(z_0) = x_0, \Im(z_0) = y_0, \Gamma, \Lambda]^T \in \mathbb{R}^4.$$

In the Karman vortex street case, there are six parameters that uniquely determine the flow field: U (the freestream flow speed), γ (the strength of each vortex in the street), a (the horizontal spacing of the vortices), h (the vertical spacing of the vortices), x_0 (the horizontal location of the vortex street relative to the sensor frame), and y_0 (the vertical location of the vortex street relative to the sensor frame). Previous work [6], demonstrated the use of arrays of pressure sensors to estimate the free-stream speed of a flow. This work assumes that flow speed has already been determined, and U is assumed to be given. As shown in the stability analysis in [11], the vertical spacing h of the vortices is directly proportional to the horizontal spacing a by $h = a\frac{1}{\pi}\sinh^{-1}(1) \approx 0.2805a$, so h can be removed from the parameter space. By using the Strouhal number St, a can also be treated as given, assuming the diameter of the upstream obstacle shedding the vortices is known. For low-frequency vortex shedding, $St = \frac{fL}{U} \approx 0.2$, where f is the frequency of shedding, L is the obstacle diameter, and U is the flow speed [17]. The frequency can be directly calculated from a and U, so if the obstacle diameter is known, then a is as well. Additionally, because the vortices move to the right with a constant speed U and are repeated to the left and right infinitely, x_0 can instead be represented by a phase angle $\phi = 2\pi\frac{x_0}{a}$, $\phi \in [-\pi, \pi)$. In this way, the parameter space is reduced to only 3 variables, so for the Karman vortex street

$$\mathbf{X}_{kvs} = [\phi, \Im(z_0) = y_0, \gamma]^T \in \mathbb{R}^3.$$

The sensor noise matrix in (6) is

$$R = \mathrm{diag}(\underbrace{R_p \ldots R_p}_{n_p}),$$

where R_p is the expected noise variance of the pressure-difference measurements.

B. Optimal Observable Path

The measurement equation and Bayesian filter framework enable estimation of the vortex parameters. To determine an optimal path for the sensor array in the vortex street case, empirical observability is used. The closed-loop control goal is to track a reference trajectory $y_{0\,\mathrm{ref}} = y_{0\,\mathrm{ref}}(\phi)$, meaning for any given ϕ with dynamics $\dot{\phi} = 2\pi U/a$, there is a reference vertical position y_0 that should be achieved by actuating the sensor array[2]. To choose the path $y_{0\,\mathrm{ref}}(\phi)$, the observability grammian W_0 is calculated along sinusoidal trajectories of varying phase and amplitude. (Only sinusoidal trajectories were examined because of the structure of the vortex street.) The local unobservability index is calculated for each trajectory according to (8). The street spacing, vortex strength, and sensor configuration match those in the experiment described in Section IV. Figure 3(a) shows the local unobservabiltiy index for each trajectory. The minima on this graph are the paths of the sensor array leading to the best estimates of the parameters $\mathbf{X}_{kvs}$. The optimal paths are shown in Fig. 3(b) in white. These are the paths that bring the vortices close to the individual pressure sensors, creating a large pressure difference among the sensor-pairs and hence a good estimate of the parameters.

For the vortex street experiment described in Section IV, the black line was chosen for $y_{0\,\mathrm{ref}}$ because it does not bring the sensors too close to the walls of the test section (indicated by the blacked dashed lines), does not bring the sensors directly in contact with the center of a vortex singularity, and has a low unobservability index as compared to the rest of the field in Fig. 3(a). The chosen path is

$$y_{0\,\mathrm{ref}} = \frac{h}{2}\cos(\phi) - \frac{h}{2}, \tag{10}$$

which takes the center of the sensor array through the center of each vortex. The reference path has the offset $-h/2$ to ensure that the midpoint of the trajectory is centered between the two parallel lines of vortices in the vortex street.

[2]Note that y_0 is the position of the vortex street in the sensor frame, so if the sensor array moves up in the inertial frame, y_0 decreases. All calculations within the estimator and controller are performed in the sensor frame. If the Karman vortex street never moves in the cross-stream direction, y_0 will still change if the sensor array moves.

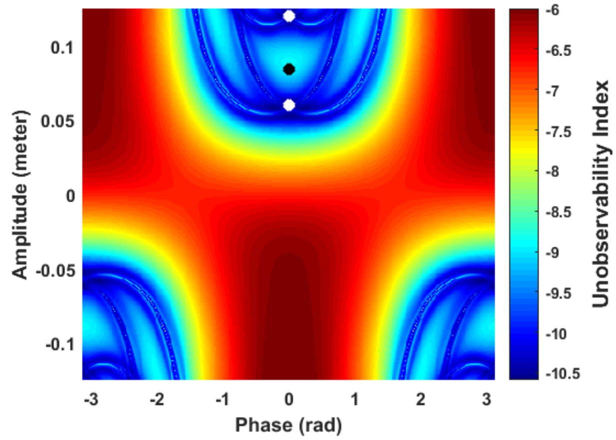

(a)

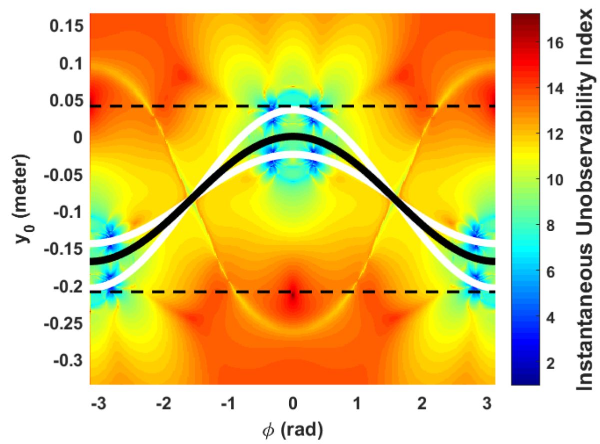

(b)

Fig. 3: (a) Local unobservability index for sinusoidal trajectories of the form Amplitude$*\cos(\phi + \mathrm{Phase}) - h/2$ through the (ϕ, y_0) plane. White circles represent minima of the test grid. Black circles represent the path followed in the experiment. (b) Instantaneous unobservability index at various points in the (ϕ, y_0) plane. White and black curves correspond to the white and black circles in (a). The dashed black lines indicate the width of the test section of the experimental setup described in Section IV.

C. Observer-Based Controller

A proportional feedback controller was chosen for both the spiral vortex experiment and the vortex street experiment. In the spiral vortex case, let k_{sv} be the gain and $\hat{x}_0$ the estimate of the vortex location relative to the sensor array. Consider

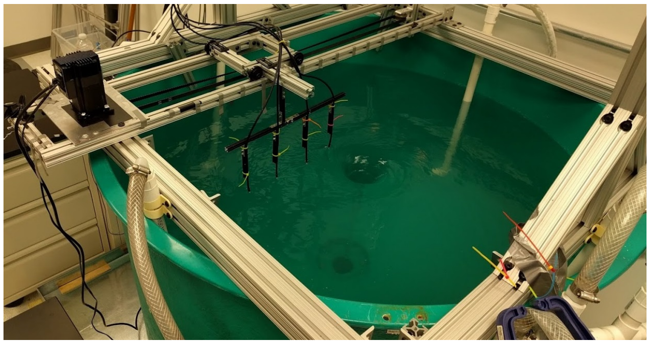

Fig. 4: The experimental testbed for the spiral vortex includes a stepper motor and belt to actuate the sensor array; the spiral vortex is centered on the drain, like a bath tub.

the proportional-control input velocity

$$u_{sv} = -k_{sv}\hat{x}_0. \tag{11}$$

Assuming velocity is being directly controlled, the closed-loop system has the continuous dynamics

$$\dot{x}_0 = u_{sv} = -k_{sv}\hat{x}_0.$$

If the estimate error is bounded, this system can be shown to be pratically stable by Lyapunov's method [18], i.e., error trajectories converge arbitrarily close to the origin (but never exactly to the origin due to the non-vanishing estimate uncertainty).

In the Karman vortex street case, let k_{kvs} be the gain, $\hat{y}_0$ the estimated cross-stream location of the primary vortex in the Karman vortex street, and $e = \hat{y}_0 - y_{0\text{ref}}$ be the error from the reference trajectory. Again, consider a proportional-control input velocity

$$u_{kvs} = -k_{kvs}e, \tag{12}$$

which yields practical stability with directly controlled velocity dynamics in y_0.

IV. Experimental Results

A. Experimental Testbeds

Figure 4 shows the first experimental testbed: a 1.2 m wide, 0.75 m deep water tub used to create a stationary spiral vortex at its center. Water exits through a drain in the bottom and is fed to three 75 watt pumps. These pumps redirect the water back into the tub where it is injected tangentially to the vortex flow through four pipes. A commercial flow-rate meter is used to directly calculate the ground truth sink strength of $\Lambda = 0.0032$ m^{2}s^{-1}. The true vortex strength, $\Gamma \approx 0.271$ m^{2}s^{-1}, is approximated by the line integral of the tangential velocity around the tub as measured by a commercial velocity meter.

A carriage sitting above the water translates in one dimension on freely spinning wheels laid in aluminum tracks. Suspended from the carriage is a rake-like structure holding the pressure sensors under the water's surface. Four Millar pressure sensors are evenly spaced over 30 cm. A stepper motor and timing belt are used to actuate the carriage across a 100 cm span. The pressure sensors are connected to a National Instruments data-acquisition board and the data are read by MATLAB.

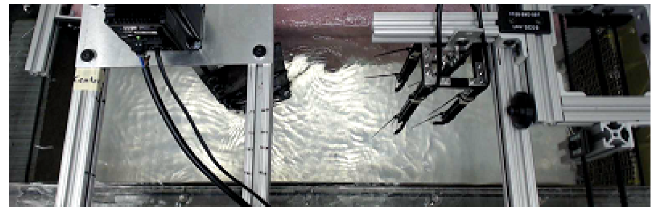

Fig. 5: The experimental testbed for the vortex street uses a stepper motor and belt to actuate the sensors. A second stepper motor actuates a flap to create the vortices. An overhead camera is used to to calculate the ground truth location of the vortices.

Estimation and control occurs as described in Section III; the control strategy in (11) uses $k_{sv} = 0.5$s^{-1}. Due to the large sample size needed from noisy pressure sensors, as well as the computational resources needed to calculate the measurement likelihood for the 151x151x25x25 matrix of possible points in the state space, a continuous-time system is not possible in the first experiment. Once the control input u_{sv} is calculated, the sensor array is translated at that velocity for one second before the next data set is taken.

Figure 5 shows the experimental testbed for the Karman vortex street. A 185 L Loligo flow tank creates a uniform 15 cm/s flow in a 88cm x 25cm x 25cm test section. A stepper motor controls a black sheet of acrylic that flaps to create vortices at the desired spacing and frequency. Through image processing, the strength of each vortex in the street was determined to be $\gamma \approx 0.0605$ m^{2}s^{-1}. A timing belt and second stepper motor control the carriage that translates the pressure sensors in the cross-stream direction. The pressure sensors are arranged in a 6cm x 6cm square and submerged under the surface of the water. A camera mounted above records the experiments in order for the ground truth of the vortex positions to be extracted after the experiment has been completed. The estimation, data aquisition, image capture, control calculation, and stepper motors are all controlled in real time from a computer running MATLAB. A course 30x30x15 grid of possible points in the (ϕ, y_0, γ) state space was used to update the estimate and control at approximately 20 Hz in order to have stable convergence to the reference trajectory. The velocity of the sensor array was controlled by the stepper motor using the control law in (12) with $k_{kvs} = 10$ s^{-1}. The vortices created by the flapper were spaced by $a = 0.6$ m, which corresponds to a hypothetical upstream obstacle of diameter 12 cm.

B. Observer-based Control Results

Open-loop surveys of the vortex tub were performed to ensure proper function of the sensors and the Bayesian filter. Figure 6 shows the survey results from using pressure sensors. Nineteen measurements were taken as the sensor array was translated from $x_0 = 44$ cm to $x_0 =$ -10 cm. Observe the symmetry about the x axis that arises from the

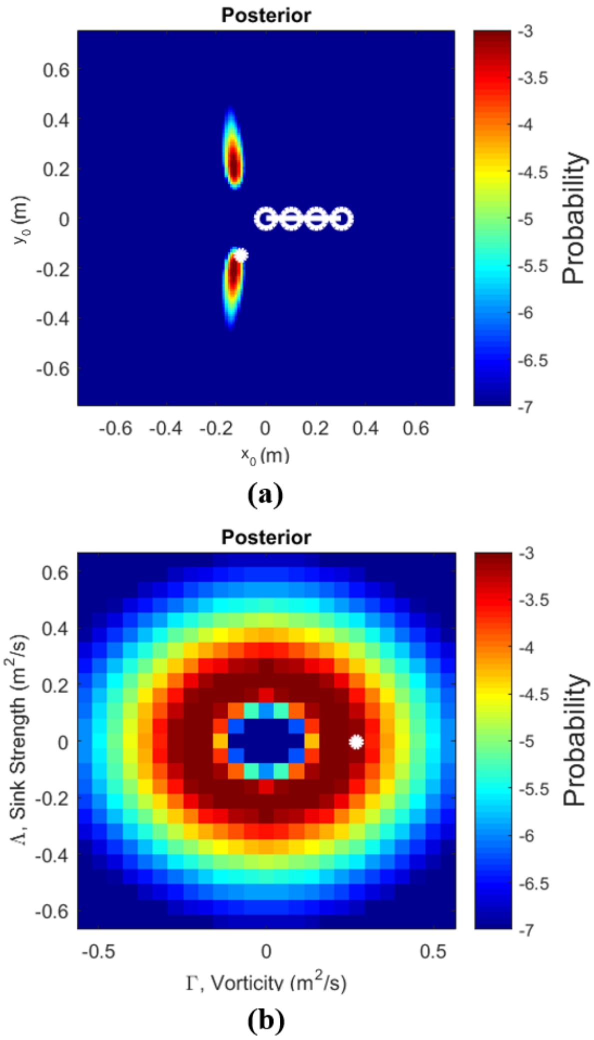

Fig. 6: Open-loop survey with $n_p = 4$ pressure sensors. The posterior marginals in the (a) (x_0, y_0) and (b) (Γ, Λ) planes. The white markings represent ground truth values.

symmetry of the sensor array. Also see that the posterior in the (Γ, Λ) plane determines only the magnitude $\Gamma^2 + \Lambda^2$, because (9) does not contain Γ or Λ in any other form.

Figure 7 shows the results from a closed-loop control test in the vortex tub using pressure sensing. The estimation was successful in calculating the x_0 coordinate of the vortex, somewhat successful in calculating the y_0 coordinate, and not very successful at calculating the $\Gamma^2 + \Lambda^2$ strength. The over-estimate of the vortex strength and the vertical distance to the vortex may also be due to the symmetry of the pressure sensor array: any given pressure-difference reading could either be from a weak vortex close by or a strong vortex far away. A square pressure sensor arrangement was chosen for the Karman vortex street experiment to avoid measurements in only one dimension and hence this issue.

Figure 8 shows the vortex street experimental results from a closed-loop experiment to track the reference trajectory given in (10). The experiment was successful in actuating the pressure sensor array to pass through each of the vortices after an initial period of larger error. The estimate of γ varies around the ground truth value, which may be explained by the small grid size along the γ axis in the state space.

Figure 9 shows the errors in the estimates of ϕ and y_0. The ground truth of y_0 matches well with the reference trajectory.

V. Conclusion

This paper describes the estimation of vortex flows and its use in closed-loop control of the flow-relative position of a sensor array inspired by lateral-line neuromasts. Measurement equations for these sensors use potential flow theory and Bernoulli's principle. The measurement equations are incorporated in a recursive Bayesian filter to estimate the planar location and strength of both a spiral vortex and Karman vortex street. Closed-loop control with pressure sensors successfully actuated the sensor array to the x_0 coordinate of the spiral vortex. An optimal path through the vortex street was determined using a metric based on the local unobservability index and tracked using closed-loop control.

In ongoing work, air bearings have been included in the vortex-street experimental setup. The direct control of the cross-stream velocity via stepper motor will be replaced with a fish-like Joukowski airfoil that will be rotated by a servo motor to create lift in the cross-stream direction. Using tools from nonlinear control, a feedback controller will take into account the flow field from the vortex street in order to slalom through the vortices on the desired trajectory.

Acknowledgments

The authors would like to thank Frank Lagor and Patrick Washington for their help in creating the experimental testbeds.

References

[1] W. J. V. Trump and M. J. McHenry, "The morphology and mechanical sensitivity of lateral line receptors in zebrafish larvae (*danio rerio*)," *The Journal of Experimental Biology*, vol. 211, 2008.

[2] S. Coombs, "Signal detection theory, lateral-line excitation patterns and prey capture behaviour of mottled sculpin," *Anim Behav*, vol. 58, no. 2, pp. 421–430, Aug 1999.

[3] A. Carrillo and M. J. McHenry, "Zebrafish learn to forage in the dark," *Journal of Experimental Biology*, vol. 219, no. 4, pp. 582–589, 2016.

[4] R. Mason, "Fluid locomotion and trajectory planning for shape-changing robots," Ph.D. dissertation, California Institute of Technology, Pasadena, California, June 2003.

[5] F. Lagor, L. DeVries, K. Waychoff, and D. Paley, "Bio-inspired flow sensing and control: Autonomous rheotaxis using distributed pressure measurements," *Journal of Unmanned System Technology*, vol. 1, no. 3, 2013.

[6] L. DeVries, F. D. Lagor, H. Lei, X. Tan, and D. A. Paley, "Distributed flow estimation and closed-loop control of an underwater vehicle with a multi-modal artificial lateral line," *Bioinspiration and Biomimetics*, vol. 10, pp. 1–15, 2015.

[7] V. I. Fernandez, "Performance analysis for lateral-line-inspired sensor arrays," Ph.D. dissertation, Massachusetts Institute of Technology, 2011.

[8] Z. Ren and K. Mohseni, "A model of the lateral line of fish for vortex sensing," *Bioinspiration & Biomimetics*, vol. 7, no. 3, p. 036016, 2012.

[9] F. D. Lagor, K. Ide, and D. A. Paley, "Touring invariant-set boundaries of a two-vortex system using streamline control," in *IEEE Conference on Decision and Control (CDC)*, Dec 2015, pp. 2217–2222.

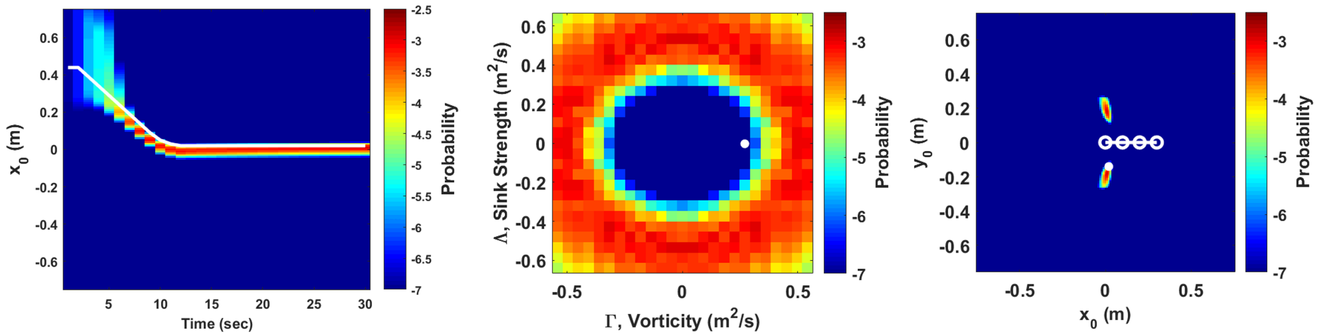

(a) **(b)** **(c)**

Fig. 7: (a) Posterior time history for x_0. The posterior marginals in the (b) (Γ, Λ) and (c) (x_0, y_0) planes. The white markings represent ground truth values.

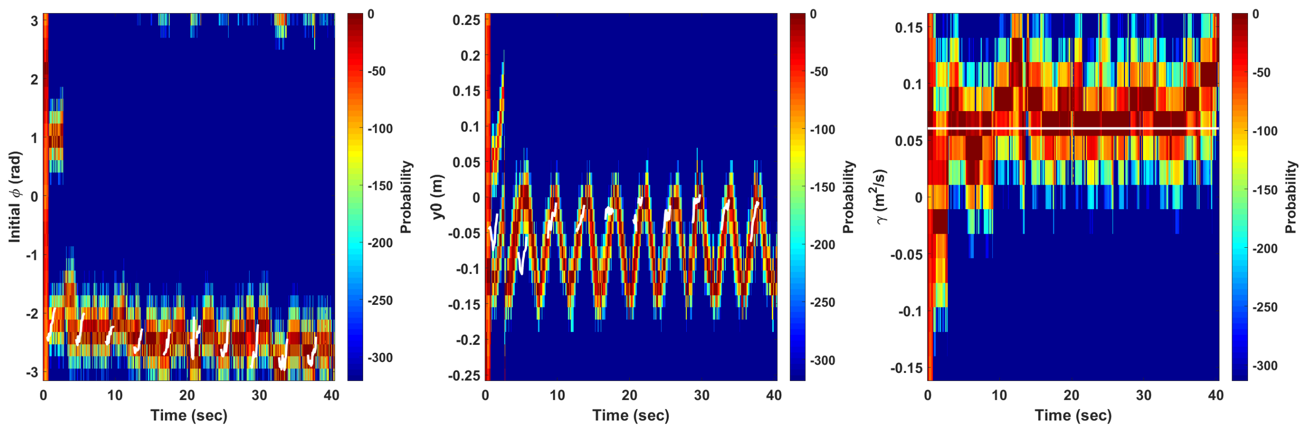

(a) (b) (c)

Fig. 8: Posterior time history for (a) the initial value of ϕ at the start of the experiment, (b) y_0, and (c) γ. (The ground truth shown in white is only extracted from the video data when the vortices were visible.)

[10] P. Y. Li and S. Saimek, "Modeling and estimation of hydrodynamic potentials," in *Decision and Control, 1999. Proceedings of the 38th IEEE Conference on*, vol. 4. IEEE, 1999, pp. 3253–3258.

[11] P. G. Saffman, *Vortex Dynamics*, G. K. Batchelor and L. B. Freund, Eds. Cambridge University Press, 1992.

[12] A. J. Krener and K. Ide, "Measures of unobservability," in *IEEE Conference on Decision and Control, held jointly with the Chinese Control Conference (CDC/CCC)*, Dec 2009, pp. 6401–6406.

[13] R. L. Panton, *Incompressible Flow*, 3rd ed. Wiley, 2005.

[14] J. D. Anderson, *Fundamentals of Aerodynamics*, 5th ed., B. Stenquist, Ed. McGraw Hill, 2007.

[15] M. S. Arulampalam, S. Maskell, N. Gordon, and T. Clapp, "A tutorial on particle filters for online nonlinear/non-Gaussian Bayesian tracking," *IEEE Transactions on Signal Processing*, vol. 50, no. 2, pp. 174–188, February 2002.

[16] B. Ćurčić-Blake and S. M. van Netten, "Source location encoding in the fish lateral line canal," *Journal of Experimental Biology*, vol. 209, no. 8, pp. 1548–1559, 2006.

[17] H. Sakamoto and H. Haniu, "A study on vortex shedding from spheres in a uniform flow," *Journal of Fluids Engineering*, vol. 112, no. 4, pp. 386–392, 1990.

[18] H. K. Khalil, *Nonlinear Control*, A. Gilfillan, Ed. Pearson, 2015.

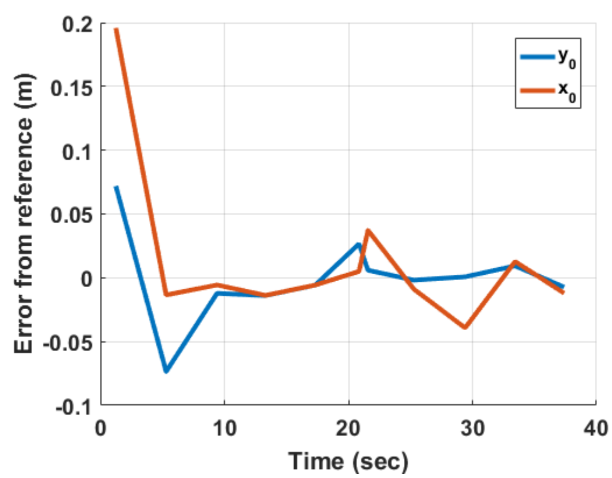

Fig. 9: Error between estimation and ground truth of x_0 and y_0 over the Karman vortex street experiment. x_0 is shown rather than the non-dimensionalized ϕ to more easily compare the errors in the two states.